

# Close-Proximity Underwater Terrain Mapping Using Learning-based Coarse Range Estimation

Bilal Arain<sup>†‡</sup>, Feras Dayoub<sup>†\*</sup>, Paul Rigby<sup>‡</sup>, Matthew Dunbabin<sup>†\*</sup>

**Abstract**—This paper presents a novel approach to underwater terrain mapping for Autonomous Underwater Vehicles (AUVs) operating in close proximity to complex 3D environments. The approach leverages a coarse learning-based scene range estimator from monocular images, which can filter transient objects such as fish and lighting aberrations. The proposed methodology then creates a probabilistic elevation map of the terrain using a learning-based scene range estimator as a sensor. The approach considers uncertainty in estimated scene range and robot pose as the AUV moves through the environment. The resulting elevation map can be used for reactive path planning and obstacle avoidance to allow robotic systems to follow the underwater terrain as closely as possible. The performance of our approach is evaluated in simulation by comparing the reconstructed terrain to ground truth reference maps in an photo-realistic underwater environment. The method is also demonstrated using field data collected within a coral reef environment by an AUV.

## I. INTRODUCTION

Dependable navigation of Autonomous Underwater Vehicles (AUVs) in close proximity to complex terrain is important for applications such as scientific image based surveys of the environment (such as coral reefs) and engineering inspections. Successful completion of these missions demands that the AUV can approach obstacles closely, while ensuring that it does not actually collide with them. A pre-requisite to this behaviour is the robust perception of obstacles and surroundings, which is the focus of this paper. Traditional acoustic sensors for terrain-based navigation are less reliable in shallow water marine environments due to distortion and scattering [1]. Thus, a reliable visual perception system is the key to detecting and avoiding obstacles at close range and with high precision. Figure 1 shows some examples of challenging coral reef environment for AUV navigation in close proximity to the complex 3D terrain.

Robust feature detection using stereo-vision is difficult due to constraints such as light absorption [2], transients such as marine life, background sun glare and motion blur [3]. We have shown in [4] that these factors can lead to falsely identified objects or free space, which may prevent robust terrain-based navigation. These limitations prevent stereo-based approaches from being used for real-time obstacle detection [5] and are primarily used for offline post-processing of the images for habitat classification [6], [7].

<sup>†</sup> Queensland University of Technology (QUT), 2 George Street, Brisbane, QLD 4000, Australia. bilal.arain@qut.edu.au.

<sup>‡</sup> The Australian Institute of Marine Science, PMB3, Townsville MC, QLD, Australia. p.rigby@aims.gov.au.

<sup>\*</sup> The Australian Research Council Centre of Excellence for Robotic Vision (ACRV). feras.dayoub@qut.edu.au, m.dunbabin@qut.edu.au.



Fig. 1: Examples of challenges for AUV navigation in close-proximity to coral reef environments. (Top) A small AUV traversing at 1.0 m above a relatively flat coral reef. (Lower left) An image from the AUV showing cluttered and dynamic (fish) obstacles. (Lower right) An image showing strong lighting variations.

In this paper, we develop an approach to underwater terrain mapping using a coarse learning-based scene range estimator from a monocular camera. We have approximated the problem of continuous range regression with a discrete range estimation problem using a monocular camera. Building on our previous work, we segment and classify the monocular images observed by the AUV into discrete obstacle ranges and show that this approach is resilient to dynamic objects (e.g. fish) and visibility aberrations. In this work, the predicted range of each image pixel, with associated uncertainty, is then used as a sensor model to construct the underwater terrain map. This probabilistic elevation map of terrain is evaluated in simulations and by using field data.

The remainder of the paper is structured as follows; Section II summarises related research in monocular-image based range estimation as classification and underwater mapping approaches for AUV applications. Section III describes the proposed methodology for terrain map generation using monocular image-based classification and uncertainty in range estimation. Section V presents results and performance analysis using field data collected during coral surveys and photo-realistic simulations, with conclusions in Section VI.

## II. RELATED WORK

Underwater terrain mapping in close proximity to obstacles requires an AUV to perform robust obstacle detection

and avoidance in real-time. Coral reef environment terrain perception could be achieved by constructing dynamic representation of the scene in terms of occupancy grids or digital elevation maps. In this paper, the relevant literature is divided into: (a) Supervised monocular image-based range estimation as classification; (b) Vision-based underwater terrain mapping for navigation.

#### A. Supervised Monocular Image-based Range Estimation as Classification

A number of techniques have been used for estimating the scene range using a monocular camera in the computer vision literature [8]. An early method to produce dense pixel depth estimates [9] used a data driven approach to learn features using a two scale network. This work has been extended by using a conditional random field (CRF) model for the scene depth regularization [10], using multi-class classification loss [11] and residual learning with reverse Huber loss function [12]. In [13], continuous scene range is transformed into a discrete number of intervals and a network is trained by ordinal regression loss to predict the range distribution. Recently, a discrete classification problem is formulated in [14] to predict a valid range probability density function (PDF) by learning the model as an independent binary classifier. This approach regularizes the model and gives better uncertainty estimates and scene depth predictions.

Although pixel-wise classification is used to estimate scene depth, there have been limited examples of range estimation for underwater obstacle avoidance using a monocular camera. For example, learning-based methods are used for habitat (coral), fauna (fish) classification [6], [7] and marine pest detection [15]. Inspired by the work in [16], we formulate the underwater discrete range prediction as a multi-modal semantic segmentation problem. In contrary to the work in [16], which predicts spatially dense range, in our method each bin covers a fixed value of a range and the labels of the bins are defined according to the range.

#### B. Vision-based Underwater Terrain Mapping for Navigation

Underwater terrain-based navigation approaches primarily focus on the localization task by estimating the state of the vehicle using onboard sensors [17]. Underwater terrain mapping-based approaches such as simultaneous localization and mapping (SLAM) build a map of the environment using a set of features identified within sonar or vision data measurements [17], [18]. Underwater navigation has been successfully demonstrated using different sensors such as stereo cameras, multibeam sonars, and Doppler Velocity Logs [6], [7].

Monocular vision-based reactive avoidance methods are proposed in [5], [19], [20] using visual perspective invariants. However, these approaches prioritise ‘escaping’ from the obstacles including marine life, while in this work we create a probabilistic elevation map of the terrain, which will enable the risk of collision to be managed. Conceptually, our approach is similar to [21], where the terrain mapping is used

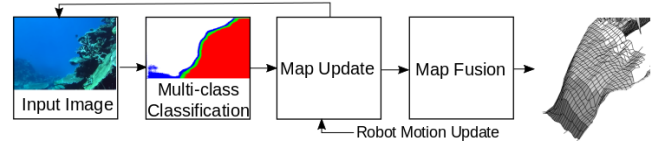


Fig. 2: Schematic overview of the terrain map generation. The multi-class classifier generates coarse range estimate of the terrain from the monocular camera in field-of-view. A probabilistic terrain map is created using the the range measurements and the robot motion update. The estimated height along with the confidence bounds are computed to produce the fused map.

for local representation of the surroundings around the robot while incorporating range estimation uncertainty to update the map. To quantify the errors in the model, epistemic and aleatoric uncertainty metrics have been used in the literature [22]. We have considered multi-modal distribution over estimated range from the semantic classifier to use as an uncertainty estimation.

### III. TERRAIN MAPPING USING LEARNING-BASED COARSE RANGE ESTIMATION

A schematic overview of the approach is shown in Figure 2. Our proposed method for terrain elevation mapping infers the range class labels in a monocular image sequence using a Deep Convolutional Neural Network (DCNN). The classifier is trained to predict the obstacles in the scene as a discrete set of ranges/distance (near, mid-field, far, or no obstacle) across the image. The predicted range of each image pixel along with its uncertainty then forms a ‘sensor model’, along with the robot motion update. A corresponding point cloud of the predicted ranges along with their associated uncertainty are then transformed to the corresponding height measurements with confidence bounds. The following sections describe in detail the approach for probabilistic underwater terrain (elevation) mapping using the semantic classes developed and used within this paper.

#### A. Terrain Map Generation

Due to the inherent difficulties of obtaining globally accurate position information without sophisticated externally introduced localisation systems, we are inspired by the work of Fankhauser [21] to generate *local* maps of the environment as the AUV traverses through it expressed as a *robot-centric* formulation.

The coordinate system used for terrain mapping is illustrated in Figure 3. The four coordinate frames are defined with an inertial frame  $I$  in NED coordinates typical for underwater environments, the base frame  $B$  that moves with the robot, a map frame  $M$  relative to the base frame, and a sensor frame  $S$  attached to the camera on the robot. The unit vectors  $\{e_x^I, e_y^I, e_z^I\}$  are along the respective inertial axes. It is assumed that there are known translation and rotation transformations  $(\mathbf{r}_{BS}, \phi_{BS})$  between the base  $B$  and the sensor  $S$  frames. The base frame  $B$  is related to the inertial frame  $I$  through the translation  $\mathbf{r}_{IB}$  and rotation  $\phi_{IB}$ .

The map is updated at each time step using the range estimation from a single image and transformed to the map frame  $M$ . In the local map frame, at each measurement step

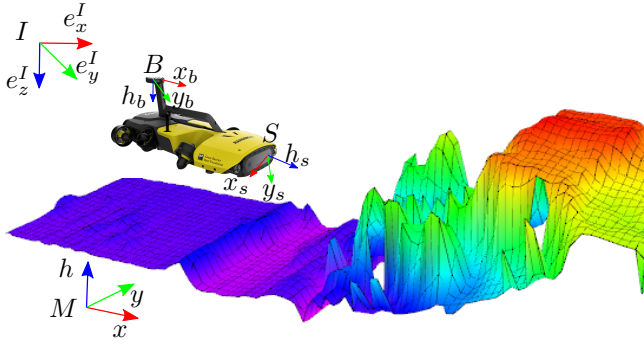


Fig. 3: Illustration of the coordinate systems used for the terrain (elevation) mapping. The inertial reference frame  $I$  is in commonly used NED coordinates, with the local right-hand map coordinate frame  $(x, y, h)$  selected to an arbitrarily selected location, and the fixed (sensing) frame  $(x_s, y_s, h_s)$  attached to the AUV.

a map cell at  $(x, y)$  is denoted by  $P_{xy} = (x, y, \hat{h})$  where  $\hat{h}$  is the estimated elevation. To obtain the estimated height from the measured elevation  $\tilde{h}$ , the measurement is approximated by Gaussian probability distribution  $\tilde{h} \sim \mathcal{N}(h_c, \sigma_{h_c}^2)$  with mean  $h_c$  and variance  $\sigma_{h_c}^2$ . The variance of the height measurement within the map  $\sigma_{h_c}^2$  is given by:

$$\sigma_{h_c}^2 = J_S \text{cov}(S) J_S^T + J_\Phi \text{cov}(\phi_{IS}) J_\Phi^T \quad (1)$$

where  $\text{cov}(S)$  is the range prediction covariance matrix of the range sensor model (see Section III-C) and  $\text{cov}(\phi_{IS})$  is the covariance matrix of the sensor rotation being a sub matrix of the  $6 \times 6$  pose covariance matrix. The Jacobians for the range predictions  $J_S$  and the sensor frame rotation  $J_\Phi$  are determined by

$$J_S = \frac{\partial h_c}{\partial s_{RSP}}, \text{ and } J_\Phi = \frac{\partial h_c}{\partial \phi_{SM}}. \quad (2)$$

The height measurement is transformed into the map frame given the position of the measurement  $s_{RSP}$  in the sensor frame, given by

$$h_c = \mathbf{P} \left( \Phi_{SM}^{-1}(s_{RSP}) - \mathbf{M} \mathbf{r}_{SM} \right), \quad (3)$$

where  $\mathbf{P} = [0 \ 0 \ 1]$  is the projection matrix to map the scalar height measurement in the map frame. The elevation measurement  $(h_c, \sigma_{h_c}^2)$  is then fused with the existing elevation map estimate  $(\hat{h}, \sigma_h^2)$  by a one-dimensional Kalman filter, given by:

$$\hat{h}^+ = \frac{\sigma_{h_c}^2 \hat{h}^- + \hat{\sigma}_h^{2-} \tilde{h}}{\sigma_{h_c}^2 + \hat{\sigma}_h^{2-}}, \quad \sigma_h^{2+} = \frac{\hat{\sigma}_h^{2-} \sigma_{h_c}^2}{\hat{\sigma}_h^{2-} + \sigma_{h_c}^2} \quad (4)$$

where estimates before and after an update are denoted by a  $-$  superscript and a  $+$  superscript respectively. A final map fusion step can be performed within the elevation mapping framework by computing the mean height  $(\hat{h}_i, h_{i_{min}}, h_{i_{max}})$  along with the confidence bounds for every cell  $i$  as the weighted mean from all cells within  $2\sigma$  confidence ellipse in the  $x - y$  plane of a cell.

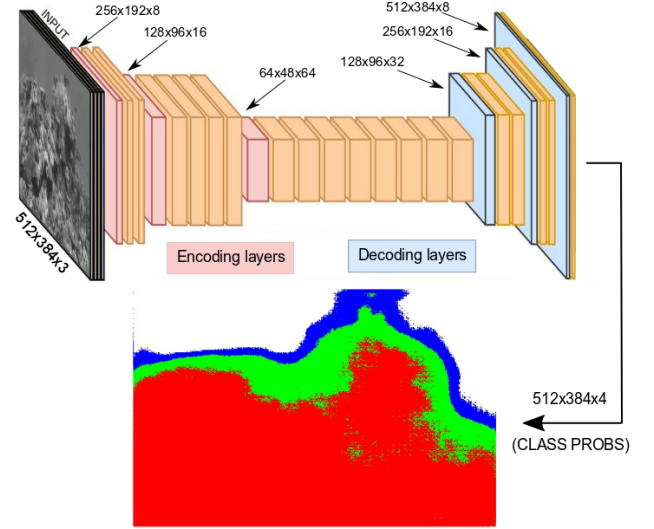


Fig. 4: The ERFNet DCNN architecture used in this work for coarse scene range estimation for an example input image and its corresponding output image in the same resolution ( $512 \times 384$ ). The resulting segmented output image is classified into 4 classes with near (red is up to 2.0 m), mid-field (green is 2.0 – 3.0 m), far (blue is 3.0 – 4.0 m) and free-space (white is  $> 4.0$  m).

To obtain the fused terrain map using (4), the values of  $\text{cov}(S)$  in (1) are required of the range sensor model. For the sake of brevity, the DCNN presented in this work is considered as a ‘sensor’ and discussed in the following sections.

### B. Coarse Range Estimation using Monocular Image Semantic Segmentation

The goal of our approach is not necessarily to faithfully reproduce fine-scale topology of the terrain, but to provide a framework which gives confidence bounds on the terrain relative to the robot for safe navigation when in close proximity to obstacles.

The detection of obstacles and their range from the camera is based on our previous work using semantic image segmentation [4]. In this work, a semantic segmentation approach is used to learn obstacles from a 2D training image set. Obstacle segmentation is considered as a multi-class,  $C+1$ , problem where obstacles are sub-divided into  $C$  classes based on their distance from the camera with everything else considered not be an obstacle.

Using the Bonnet toolkit [23], a model based on the variable receptive field non-bottleneck concept of ERFNet [24] is employed. This is achieved through factorized convolutions of diverse receptive fields. In this work, 4 convolutional layers of increasing complexity,  $K = [8; 16; 32; 64]$ , are used as illustrated in Figure 4 to produce a segmented obstacle range image. Full images are passed to the network with the output being a pixel wise prediction of obstacle range consisting of  $C = 3$  obstacle classes based on their distance from the camera (near, mid-field and far), and a final obstacle free-space class.

In this work, we use the semantic image segmentation to obtain coarse range and height estimates of the terrain in



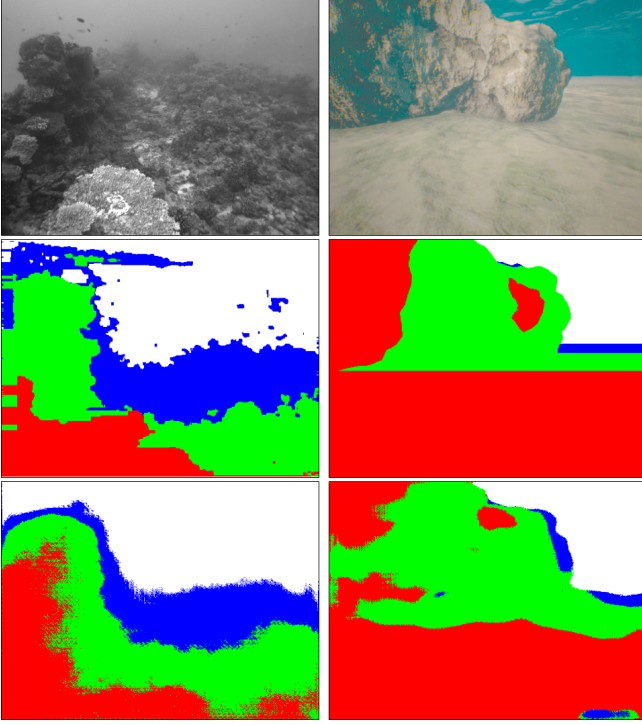


Fig. 5: Example results of image segmentation for a scene from a real coral reef (left column), and the simulated reef (right column). The top row is the input image to the classifier, the middle row is the “true” binned range estimate obtained from a stereo camera, and the lower row is the prediction from a monocular camera. The colors represent the predicted obstacle range based on training images (i.e. red is near, green is mid-field, blue is far and free-space is white).

front of the robot. Figure 6 illustrates the key parameters with reference to the local map frame, where the map elevation for an arbitrary cell is estimated as  $\hat{h}(x, y)$ . At each time instance, a semantically labelled image is produced that predicts the scene regions within each class range referenced to the sensor frame. Using the intrinsic camera parameters, each pixel  $u, v$  in each class is transformed to an elevation ( $h_{c_j}$ ) in the map frame using (3) for each local map cell  $i$ . The uncertainty of the class prediction is also used to update the associated map cell.

As the scene is classified into four range classes and the exact topology between the class boundaries is not known nor available (assuming only a monocular camera), it is difficult to determine the exact height to update the local map within each class boundary. Therefore, we update the elevation in the local map for only those pixels along the top of the predicted class boundary (as shown in Figure 6). It can be hypothesised that in a typical underwater scene, the class boundary is at its closest to the actual range bin value. An evaluation of these range estimation and map update cases is given in Section V. The sensor covariance matrix is obtained from the class uncertainty in the predicted ranges, which is discussed in the next section.

### C. Class Uncertainty Prediction

The probabilistic mapping framework employed in this paper, (see Section III-A), requires an estimate of the uncertainty in the coarse range predictions from the DCNN.

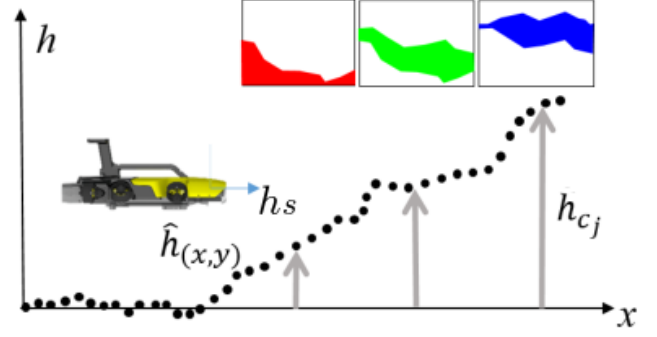


Fig. 6: Illustration of the key terrain (elevation) map parameters referenced to the map coordinate system. Multi-class range of objects in the near-field (red), mid-field (green) and far-field (blue) is transformed to an elevation in the map frame.

To obtain the class prediction uncertainty, the distribution of predicted classes are used from the output of the network as illustrated in Figure 4.

We have used variance in the prediction of our deep neural network as a range sensor model uncertainty to improve the estimated height of each cell in generating the terrain map. To quantify the uncertainty using the class probability distribution from the classifier, the range mean and variance are computed by

$$\mu_z = \sum_{i=1}^4 r_{z_i} P(r_i) \quad (5)$$

$$\sigma_z^2 = \sum_{i=1}^4 (r_{z_i} - \mu_z)^2 P(r_i) \quad (6)$$

where  $r_{z_i}$  is the predicted range of class  $i$ ,  $P(r_i)$  is the corresponding probability distribution of the predicted classes,  $\mu_z$  and  $\sigma_z^2$  are the mean and variance of the probability distribution for each pixel in the resulting segmented output image respectively. Note that the covariance of the range sensor model  $\text{cov}(S) = [0 \ 0 \ \sigma_z^2]$  in (1) is  $3 \times 3$  diagonal matrix and is updated for each pixel of the resulting segmented image over an estimated range, which is different to the previously used range sensor models in [21], [25]. Figure 7 illustrates an example class uncertainty estimation for an input image.

## IV. EXPERIMENTAL SETUP

To facilitate evaluation of the algorithms and approaches within this paper, a custom photo-realistic underwater simulation environment was developed within Microsoft Air-Sim [26]. The simulator is built using various off-the-shelf Unreal Marketplace components to create underwater lighting model and photo-realistic scenes of rocky 3D underwater structures suitable for complex terrain mapping. A model of small ROV was integrated with a custom camera model similar to that used on AUVs. Example images of a simulated 3D scene and an image from the AUV’s simulated camera are shown in Figures 5 and 8 respectively.

In order to evaluate the performance of the resulting terrain map using the proposed methodology, stereo image datasets



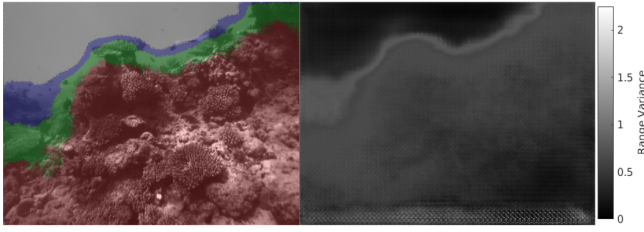


Fig. 7: (Left) Original reef image with predicted binned ranges overlaid for comparison, and (Right) the calculated variance, normalised and converted to a grayscale image for visualisation. The colors represent the predicted obstacle range based on training images (i.e. red is near, green is mid-field, blue is far and free-space is white). The range variance is scaled from zero (black) to maximum 2.25 (white). Note that the free space class range is set to 5.0 m, which gives us the maximum mean range of 3.5 m and the maximum range variance of 2.25.

were collected during coral reef surveys at John Brewer reef in the Great Barrier Reef. The images were collected using the RangerBot AUV [27], shown in Figure 3 and Figure 6. The AUV is built around two stereo camera pairs (forward and downward). The downward stereo pair has a camera baseline of 75 mm, with the forward stereo camera pair having a baseline of 120 mm. All image processing and data capturing runs on-board the AUV using an NVIDIA Jetson TX2 module as the primary computation capability. In order to train the proposed classifier for what is considered ‘appropriate’ obstacles for the coral survey tasks, the AUV was programmed to capture images using the front stereo pairs with AUV manually guided over suitable locations around the complex reef terrain.

## V. RESULTS

### A. Coarse Range Estimation

Two networks were trained for this work; one using the simulator generated images (see Section V-B), and another using field data collected on the Great Barrier Reef. For the simulation analysis, a custom photorealistic underwater environment was created using the Unreal Game Engine. Within this environment, a simulated underwater robot with cameras was used to generate an image sequence (see Figure 8). Using the simulator, annotated training images were generated by ray-tracing each pixel in the simulated camera image to the obstacle to obtain its range then discretising the range into  $C = 3$  classes which correspond to near ( $\tau_m - 2.0$  m), mid-field (2.0 – 3.0 m), far (3.0 – 4.0 m) and a forth class being free-space ( $> 4.0$  m). The parameter  $\tau_m$  is the minimum effective detection distance from the obstacle, which for the experimental data is 45 cm. Training of the field model followed a similar approach with the range classes obtained by stereo matching as describe in [4]. A total of 807 simulation annotated images and 50 field annotated images were used to train the respective models (see [4] for performance details of the field model). Figure 5 shows examples of a training image, their corresponding class annotations, and the predicted segmentation for both a real (field) and a simulated scene.



Fig. 8: An example 3D scene from the photo-realistic simulator used for evaluating the probabilistic terrain mapping methodology. The robotic system is shown as a scale guide (0.5m x 0.5m) and is pointed in the direction of travel over the 3D structure.

Table 1 summarizes the quantitative performance of the coarse range estimation using multi-class classifier in terms of the mean accuracy of all classes and the Intersection over Union metrics (IoU). The models were trained with images of size  $512 \times 384$  pixels using the median frequency loss with a learning rate of  $10^{-3}$ . The tuning parameters  $\gamma$  [28] and  $\epsilon$  [29] were set to 2 and  $10^{-8}$  respectively. To evaluate the generality of the proposed range estimation approach, a model trained on 50 images of the reef from our previous work [4], was applied to the images collected using the RangerBot AUV. The simulated training images had a mean accuracy of 0.935 and mean IoU of 0.753 and the corresponding test set result in a mean accuracy of 0.777 and mean IoU of 0.474. It is believed that the artifacts in the simulated ground truth images, due to change in artificial lighting conditions, within the Unreal simulation environment has contributed to potential confusion between the predicted classes.

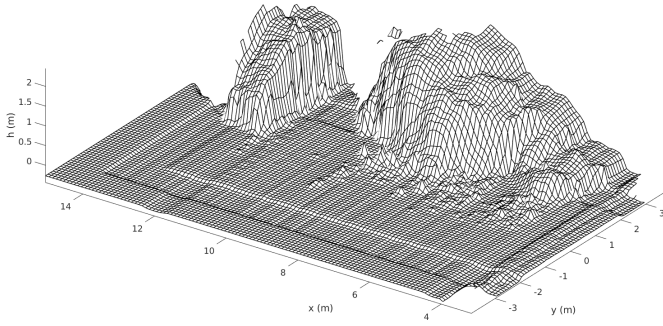
### B. Evaluation in Simulations

To evaluate the proposed methodology, two simulations were carried out to investigate scenarios where the structure is primarily to the side or below the robot. The main motivation behind using a fixed monocular forward camera is to employ the proposed methodology for the commercial-off-the-shelf (COTS) vehicles such as Blue Robotics BlueROV2 [30]. The integration of additional sensors, other than the forward camera, to the COTS platforms require significant modifications and at times is not possible.

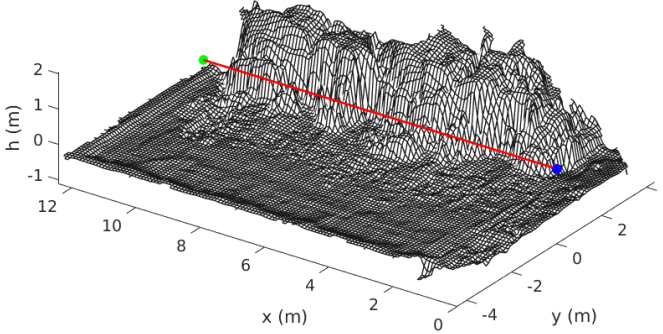
In both simulations, the robot flies across the transect along x-axis from 0.0 m to 12.0 m at constant  $h = 1.0$  m and  $y = 0.0$  m. In simulation 1, the terrain is higher than the

TABLE I: Coarse Range Estimation Performance.

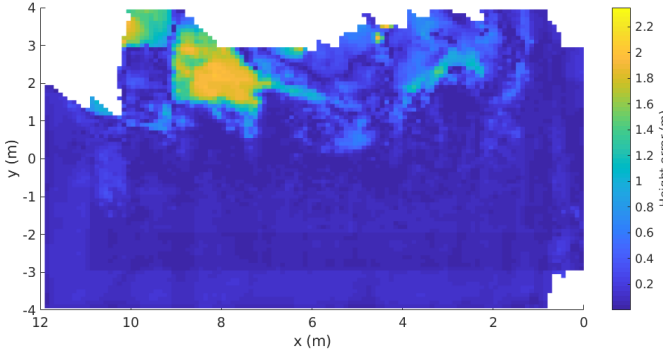
Simulations				
Number of samples	Mean Accuracy		Mean IoU	
Training	Validation	Test	Validation	Test
284	0.935	0.777	0.753	0.474
Experiments				
Number of samples	Mean Accuracy		Mean IoU	
Training	Validation	Test	Validation	Test
50	0.844	0.791	0.671	0.627



(a) Example of 3D occupancy grid of the simulator terrain used as a ground truth for algorithm evaluation.



(b) Example of the predicted map when accounting for the classification uncertainty. The robot traversed across the transect (red) at a constant  $h = 1.0$  m from start point (blue marker) to end point (green marker) along the x-axis, while y-axis was set to zero.



(c) Error between the predicted terrain map compared to the ground truth map (top) to quantify the classifier performance.

Fig. 9: Example of the simulation 1 scenario for an AUV to follow the transect line in close proximity to the unknown terrain. Note the robot-centric terrain map has been transformed to the global coordinate frame to allow comparison with the ground truth map.

AUV traverse height, where as in simulation 2, it is below the AUV. It is expected that the discretized visual information, relating to the distance from the fixed forward monocular camera, projected onto the surface, resulted in invisible areas (white spaces). The two simulator terrains used as a ground truth for algorithm evaluations are shown in Figure 9a and Figure 11a. The results presented in this section are evaluated based on the predicted terrain to map the obstacles in close proximity to the terrain.

Figure 9b illustrates how the terrain in simulation 1 was predicted using range classification, when accounting for the range uncertainty using a monocular camera. Comparison be-

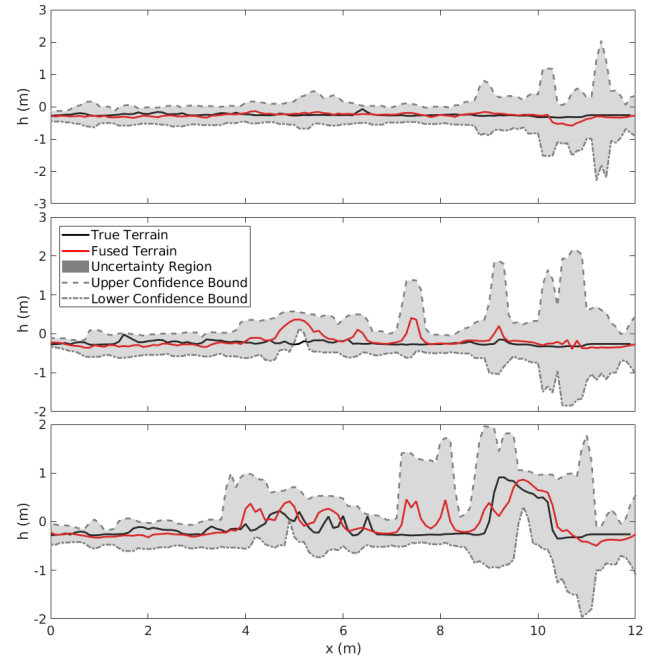


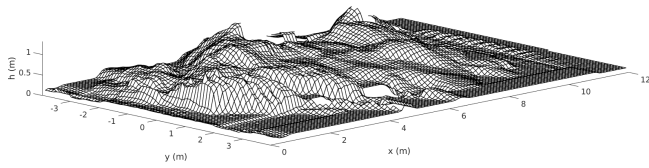
Fig. 10: The cross section view of the contour terrain map in the vehicle direction (Top), at 0.5 m (Middle), and at 1.0 m (Lower) in the y-axis showing the comparison between resulting predicted terrain and the true terrain along with the estimated upper and lower confidence bounds. Note that the ground truth offset height has been shifted to the initial robot-centric pose.

tween the ground truth terrain in Figure 9a and the predicted terrain shows that there was a maximum height error of 2.2 m approximately, shown in Figure 9c. Lack of observation of the ‘gap’ between two terrain structures resulted in the height error that was due to binning of the predicted classes at fixed ranges. This error could be minimized by either adding more classes to estimate the ranges at finer distances or to employ range estimation methodologies using coarse-to-fine networks [14].

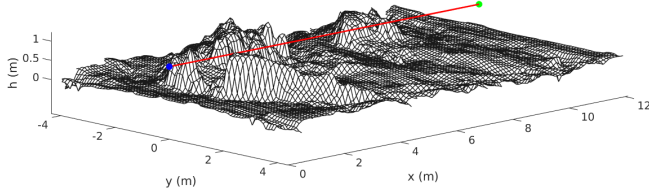
Figure 10 is the cross sectional view of the predicted terrain map shown in Figure 9b in the y-axis at 0.0 m (along the transect), 0.5 m, and 1.0 m. The maximum error between the predicted terrain and the true terrain along the transect is 25.0 cm approximately. The cross-section to the side of the terrain, while robot traversing through the environment, provides us the indication of the use case for close-proximity surveying tasks. Overall, the results show that the maximum predicted height confidence bounds resulted in 2.0 m approximately due to the mismatch between the true terrain and the predicted terrain. In future, we aim to use the confidence bounds as a ‘safety margin’ for local path planning.

In simulation 2, the AUV was tasked to travel above the terrain at constant  $h = 1.0$  m. Figure 11b illustrates how the terrain was predicted using a fixed forward monocular camera. Figure 11c shows a maximum height error of 1.0 m in comparison to the true terrain. It can be seen in Figure 11c that the maximum error for a (yellow) patch of approximately 10 cm to the 4.0 m left of the robot traverse direction was observed.

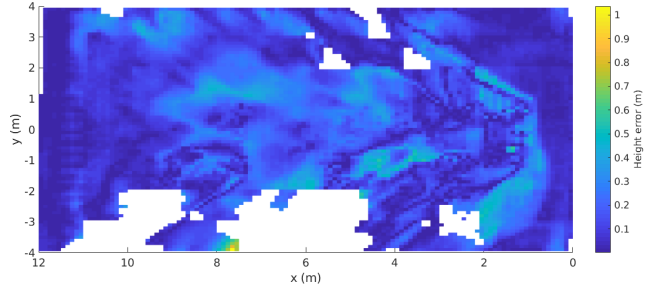
Figure 12 is the cross sectional view of the terrain shown



(a) Example of 3D occupancy grid of the simulator terrain used as a ground truth for algorithm evaluation.



(b) Example of the surface terrain map generated using the proposed approach when accounting for the classification uncertainty. The robot traversed across the transect (red) at a constant  $h = 1.0$  m from start point (blue marker) to end point (green marker) along the x-axis, while y-axis was set to zero.



(c) Error between the predicted terrain map compared to the ground truth map (top) to quantify the classifier performance. Note that the white spaces are unobserved regions when using a fixed monocular forward camera.

Fig. 11: Example of the simulation 2 scenario for an AUV to follow the transect line in close proximity to the unknown terrain. Note the robot-centric terrain map has been transformed to the global coordinate frame to allow comparison with the ground truth map.

in Figure 11b in the robot travelling direction ( $y = 0.0$  m), and at  $y = \pm 0.5$  m of the transect. Figure 12 shows that the maximum error between the predicted terrain, when accounting for the classification uncertainty, and the true terrain in the vehicle traverse direction is 30.0 cm approximately.

### C. Experimental Evaluation using Real-World Data

The performance of the multi-class classifier-based underwater terrain mapping approach was evaluated using image data sets collected by the RangerBot AUV during surveys at John Brewer Reef. The RangerBot AUV is equipped with the forward stereo camera pair. Only the left camera image data sets from the AUV's forward stereo pair was used for performance evaluation to verify the predicted coral reef terrain map. The experimental results are shown in Figure 13 with the robot trajectory around the complex reef terrain. The ability of the proposed multiclass classifier for range prediction with uncertainty can be clearly seen to generate a 3D representation of the scene using a monocular camera for coral reef surveys. To evaluate the performance of the range estimation qualitatively, an example of snapshots (markers) at a regular interval of approximately 8.0 s is

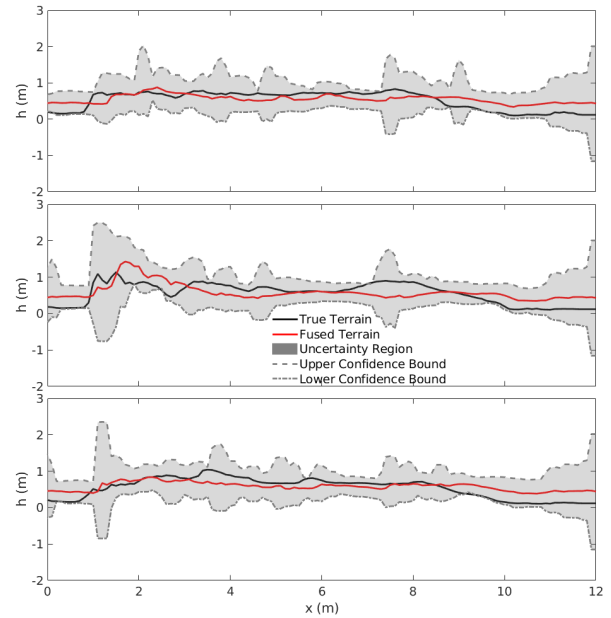
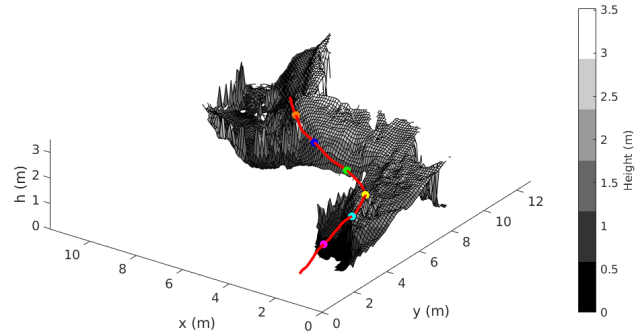


Fig. 12: The cross section view of the surface terrain map in the vehicle direction (Top), at 0.5 m (Middle), and at  $-0.5$  m (Lower) in the y-axis showing the comparison between resulting predicted terrain and the true terrain along with the estimated upper and lower confidence bounds. Note that the ground truth offset height has been shifted to the initial robot-centric pose.



(a) An example of generated terrain map from coral reef survey at John Brewer reef environment. The RangerBot AUV trajectory is shown in red, along with the markers (input images) at different locations along the trajectory.

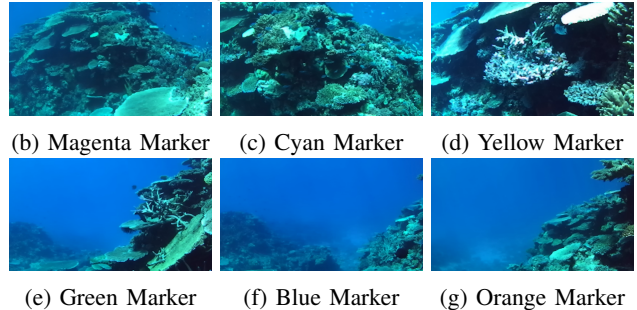


Fig. 13: Results of predicted terrain map generated while following the coral reef terrain at John Brewer reef.

shown in Figure 13b–13g. As can be seen, the approach reliably predicts the range and acutely reproduces the relative 3D terrain map in front of the camera. These results show promise for providing robust obstacle maps for use in real-



time AUV path planning applications, particularly for low-altitude coral surveys.

## VI. CONCLUSIONS

This paper has presented a novel underwater terrain mapping approach using monocular semantic image segmentation. Two DCNNs were trained using simulated and real world stereo imagery; these were then used to produce a probabilistic terrain map from images collected during low-altitude coral reef surveys. The prediction output of the multi-class classifier, representing the range of obstacles along with its uncertainty, was transformed to a probability density function of range measurements. The probabilistic range estimate, along with the robot motion update, was used to generate an estimated height map including confidence bounds. The method was evaluated using a photo-realistic simulated environment, and with field data collected by an AUV. The simulations and field results show that the proposed approach is viable for obstacle detection and range estimation using a monocular camera in reef environments. Future work will use the predicted terrain map for local path planning in order to follow the underwater coral reef terrain as closely as possible for surveying tasks.

## REFERENCES

- [1] A. Marouchos, B. Muir, R. Babcock, and M. Dunbabin, "A shallow water auv for benthic and water column observations," in *OCEANS 2015-Genova*. IEEE, 2015, pp. 1–7.
- [2] M. Roser, M. Dunbabin, and A. Geiger, "Simultaneous underwater visibility assessment, enhancement and improved stereo," in *IEEE Conference on Robotics and Automation*. IEEE, 2014, pp. 3840–3847.
- [3] M. Dunbabin, P. Corke, and G. Buskey, "Low-cost vision-based auv guidance system for reef navigation," in *Robotics and Automation, 2004. Proceedings. ICRA'04. 2004 IEEE International Conference on*, vol. 1. IEEE, 2004, pp. 7–12.
- [4] B. Arain, C. McCool, P. Rigby, D. Cagara, and M. Dunbabin, "Improving underwater obstacle detection using semantic image segmentation," in *International Conference on Robotics and Automation (ICRA)*. IEEE, 2019, pp. 9271–9277.
- [5] F. G. Rodríguez-Teiles, R. Pérez-Alcocer, A. Maldonado-Ramírez, L. A. Torres-Méndez, B. B. Dey, and E. A. Martínez-García, "Vision-based reactive autonomous navigation with obstacle avoidance: Towards a non-invasive and cautious exploration of marine habitat," in *IEEE Conference on Robotics and Automation*. IEEE, 2014, pp. 3813–3818.
- [6] S. B. Williams, O. Pizarro, J. M. Webster, R. J. Beaman, I. Mahon, M. Johnson-Roberson, and T. C. Bridge, "Autonomous underwater vehicle-assisted surveying of drowned reefs on the shelf edge of the great barrier reef, australia," *Journal of Field Robotics*, vol. 27, no. 5, pp. 675–697, 2010.
- [7] S. B. Williams, O. R. Pizarro, M. V. Jakuba, C. R. Johnson, N. S. Barrett, R. C. Babcock, G. A. Kendrick, P. D. Steinberg, A. J. Heyward, P. J. Doherty *et al.*, "Monitoring of benthic reference sites: using an autonomous underwater vehicle," *IEEE Robotics & Automation Magazine*, vol. 19, no. 1, pp. 73–84, 2012.
- [8] A. Bhoi, "Monocular depth estimation: A survey," *arXiv preprint arXiv:1901.09402*, 2019.
- [9] D. Eigen, C. Puhrsch, and R. Fergus, "Depth map prediction from a single image using a multi-scale deep network," in *Advances in neural information processing systems*, 2014, pp. 2366–2374.
- [10] B. Li, C. Shen, Y. Dai, A. Van Den Hengel, and M. He, "Depth and surface normal estimation from monocular images using regression on deep features and hierarchical crfs," in *Proceedings of the IEEE conference on computer vision and pattern recognition*, 2015, pp. 1119–1127.
- [11] Y. Cao, Z. Wu, and C. Shen, "Estimating depth from monocular images as classification using deep fully convolutional residual networks," *IEEE Transactions on Circuits and Systems for Video Technology*, vol. 28, no. 11, pp. 3174–3182, 2017.
- [12] I. Laina, C. Rupprecht, V. Belagiannis, F. Tombari, and N. Navab, "Deeper depth prediction with fully convolutional residual networks," in *2016 Fourth international conference on 3D vision (3DV)*. IEEE, 2016, pp. 239–248.
- [13] H. Fu, M. Gong, C. Wang, K. Batmanghelich, and D. Tao, "Deep ordinal regression network for monocular depth estimation," in *Proceedings of the IEEE Conference on Computer Vision and Pattern Recognition*, 2018, pp. 2002–2011.
- [14] G. Yang, P. Hu, and D. Ramanan, "Inferring distributions over depth from a single image," in *International Conference on Intelligent Robots and Systems (IROS)*, 2019.
- [15] F. Dayoub, M. Dunbabin, and P. Corke, "Robotic detection and tracking of crown-of-thorns starfish," in *Intelligent Robots and Systems (IROS), 2015 IEEE/RSJ International Conference on*. IEEE, 2015, pp. 1921–1928.
- [16] S. McMahon, N. Sunderhauf, B. Upcroft, and M. Milford, "Multi-modal trip hazard affordance detection on construction sites," *IEEE Robotics and Automation Letters*, no. 1, 2018.
- [17] J. Melo and A. Matos, "Survey on advances on terrain based navigation for autonomous underwater vehicles," *Ocean Engineering*, vol. 139, pp. 250–264, 2017.
- [18] L. Paull, S. Saeedi, M. Seto, and H. Li, "Auv navigation and localization: A review," *IEEE Journal of Oceanic Engineering*, vol. 39, no. 1, pp. 131–149, 2014.
- [19] A. Maldonado-Ramírez, L. A. Torres-Méndez, and F. Rodríguez-Telles, "Ethologically inspired reactive exploration of coral reefs with collision avoidance: Bridging the gap between human and robot spatial understanding of unstructured environments," in *IEEE/RSJ Conference on Intelligent Robots and Systems*. IEEE, 2015, pp. 4872–4879.
- [20] P. Drews, E. Hernández, A. Elfes, E. R. Nascimento, and M. Campos, "Real-time monocular obstacle avoidance using underwater dark channel prior," in *Intelligent Robots and Systems (IROS), 2016 IEEE/RSJ International Conference on*. IEEE, 2016, pp. 4672–4677.
- [21] P. Fankhauser, "Perceptive locomotion for legged robots in rough terrain," Ph.D. dissertation, ETH Zurich, 2018.
- [22] A. Kendall and Y. Gal, "What uncertainties do we need in bayesian deep learning for computer vision?" in *Advances in neural information processing systems*, 2017, pp. 5574–5584.
- [23] A. Milioto and C. Stachniss, "Bonnet: An open-source training and deployment framework for semantic segmentation in robotics using cnns," *arXiv preprint arXiv:1802.08960*, 2018.
- [24] E. Romera, J. M. Alvarez, L. M. Bergasa, and R. Arroyo, "Erfnet: Efficient residual factorized convnet for real-time semantic segmentation," *IEEE Transactions on Intelligent Transportation Systems*, vol. 19, no. 1, pp. 263–272, 2018.
- [25] C. V. Nguyen, S. Izadi, and D. Lovell, "Modeling kinect sensor noise for improved 3d reconstruction and tracking," in *2012 second international conference on 3D imaging, modeling, processing, visualization & transmission*. IEEE, 2012, pp. 524–530.
- [26] S. Shah, D. Dey, C. Lovett, and A. Kapoor, "Airsim: High-fidelity visual and physical simulation for autonomous vehicles," in *Field and service robotics*. Springer, 2018, pp. 621–635.
- [27] M. Dunbabin, F. Dayoub, R. Lamont, and S. Martin, "Real-time vision-only perception for robotic coral reef monitoring and management," in *ICRA Workshop on Underwater Robotics Perception*. IEEE, 2019.
- [28] T.-Y. Lin, P. Goyal, R. Girshick, K. He, and P. Dollár, "Focal loss for dense object detection," *IEEE transactions on pattern analysis and machine intelligence*, 2018.
- [29] D. P. Kingma and J. Ba, "Adam: A method for stochastic optimization," *arXiv preprint arXiv:1412.6980*, 2014.
- [30] Blue Robotics, "BlueROV2," <https://bluerobotics.com/store/rov/bluerov2>, 2019.